


Collective flow at SIS energies within a hadronic transport approach: Influence of light nuclei formation and equation of state

J. Mohs ^{1,2} M. Ege,² H. Elfner ^{3,2,1} and M. Mayer²

¹Frankfurt Institute for Advanced Studies, Ruth-Moufang-Strasse 1, 60438 Frankfurt am Main, Germany

²Institute for Theoretical Physics, Goethe University, Max-von-Laue-Strasse 1, 60438 Frankfurt am Main, Germany

³GSI Helmholtzzentrum für Schwerionenforschung, Planckstr. 1, 64291 Darmstadt, Germany



(Received 13 January 2021; revised 4 August 2021; accepted 22 February 2022; published 21 March 2022)

Collective flow observables are known to be a sensitive tool to gain insights on the equation of state of nuclear matter from heavy-ion collision observations. Towards more quantitative constraints one has to carefully assess other influences on the collective behavior. In this work a hadronic transport approach SMASH (simulating many accelerated strongly interacting hadrons) is applied to study the first four anisotropic flow coefficients in Au + Au collisions at $E_{\text{lab}} = 1.23A$ GeV in the context of the recently measured data by the HADES Collaboration. In particular, the formation of light nuclei is important in this energy regime. Two different approaches are contrasted to each other: A clustering algorithm inspired by coalescence as well as microscopic formation of deuterons via explicit cross sections. The sensitivity of directed and elliptic flow observables to the strength of the Skyrme mean field is explored. In addition, it is demonstrated that the rapidity-odd v_3 coefficient is practically zero in this energy regime and the ratio of v_4/v_2^2 is close to the value of 0.5 expected from hydrodynamic behavior. This study establishes the current understanding of collective behavior within the SMASH approach and lays the ground for future more quantitative constraints on the equation of state of nuclear matter within improved mean-field calculations.

DOI: [10.1103/PhysRevC.105.034906](https://doi.org/10.1103/PhysRevC.105.034906)

I. INTRODUCTION

In heavy-ion collisions the anisotropy of the particle production in the transverse plane is described in terms of flow coefficients. In transport calculations flow observables were shown to be very sensitive to nuclear potentials and the equation of state (EoS) [1,2]. Hence one can put constraints on the EoS by comparing hadronic transport calculations with experimental flow data.

Depending on the active degrees of freedom in the different transport approaches, different conclusions about the strength of the mean-field interactions are drawn. Approaches mainly based on nucleons and pions with sophisticated potentials including momentum-dependent interactions as described in Refs. [3,4] come to the best agreement with the wealth of existing FOPI data [5], when mean fields corresponding to a “soft” equation of state are employed [6–8]. The nuclear potential depends on the relative momentum as p - A experiments show and the subthreshold production of kaons is best described with soft momentum-dependent potentials [9]. In transport approaches where the mean fields lacks a momentum dependence, a hard EoS was found to agree with the data [10–12]. This is similar in recent approaches with many resonance states like UrQMD that arrive at the same quality of agreement with experimental data upon incorporating potentials corresponding to a “hard” equation of state [13–15]. Modifying the equation of state via modifications of the collision term offers an orthogonal avenue to study collective behavior within transport approaches [16].

The nuclear equation of state at high densities is relevant also for the dynamical description of neutron-star mergers. After the first detection of gravitational wave signals [17], there is a large interest in sophisticated theoretical calculations of their detailed evolution which is relevant for the nucleosynthesis including different assumptions about the equation of state of QCD matter at high densities (see Refs. [18,19] for recent examples). Despite the isospin difference that is encoded in the symmetry energy that can also be extracted from heavy-ion reactions [20,21], further knowledge on the equation of state is important. Before a quantitative extraction of the equation of state, including uncertainty quantification using Bayesian techniques, is sensible, all possible systematic uncertainties in the transport approaches need to be understood. One of those is the formation of light clusters that incorporates about 35% of the nucleons in heavy-ion reactions at SIS-18 energies (see Fig. 41 in Ref. [22]). Models based on a quantum-mechanical calculations where the coalescence of nucleons is catalyzed by the surrounding nuclear matter [23], calculations in momentum space [24,25], statistical coalescence in a fireball model [26,27], a model applying the density-matrix approach [28], and coalescence models based on phase-space separation in the final state of a transport calculation [29] have been devised. In addition, more comprehensive dynamical approaches [30,31] have been developed. Using coalescence, protons and deuterons are predicted to follow a constituent number scaling [15].

In this work we assess how SMASH (simulating many accelerated strongly interacting hadrons) [32,33] performs

compared with recent measurements of flow coefficients at SIS-18 energies [34,35] with a rather simple Skyrme parametrization of the EoS [36] and investigate the sensitivity of the results to the stiffness of the EoS. This is meant as a baseline for further calculations employing more sophisticated mean-field implementations such as the one in Ref. [37]. The main emphasis in this work is on exploring different treatments for light nuclei production, which constitutes one of the major uncertainties. We concentrate on the most abundant and lightest nucleus, namely, the deuteron, and compare two different ways of taking the light nuclei formation into account. Coalescence of nucleons in the final state as described in Ref. [29] is contrasted to the dynamical treatment by producing and propagating deuterons throughout the evolution of a heavy-ion collision, as described in Ref. [38].

The paper is structured as follows: First the SMASH transport with the current state of nuclear potentials present in the calculation and the different ways of treating light nuclei formation is described in Sec. II. Then, the effects of different Skyrme parameters and light nuclei treatments on the directed flow in Sec. III and of elliptic flow in Sec. IV of nucleons and deuterons are evaluated. Afterward, the evolution over time of the directed and elliptic flow is studied in Sec. V. Finally, we present some higher flow coefficients and show v_3 computed with the scalar product method and the ratio of v_4/v_2^2 in Sec. VI. Finally, we conclude and present an outlook in Sec. VII.

II. SMASH WITH POTENTIALS AND LIGHT NUCLEI PRODUCTION

A. Hadronic transport with mean field

In this work, we apply the transport approach SMASH [32,33] to calculate flow observables. The approach is based on the Boltzmann equation with hadronic degrees of freedom. Starting with nuclei sampled from a Woods-Saxon distribution, hadrons are explicitly propagated between interactions. At low collision energies most inelastic collisions form resonances with properties adopted from Ref. [39]. For the resonances, the spectral functions are described by relativistic Breit-Wigner distributions without medium modification. The mass dependence of the decay width is included according to Ref. [40].

For the propagation between the interactions nuclear potentials are optionally taken into account. Let us note here that, for the current work, we stick with the simple Skyrme potential without momentum dependence, since this is the same setup that has been used in other recent works in comparable approaches [14] and the default parameters have been determined in a comparison between multiple different transport codes [36].

At this point the Skyrme and symmetry potential are present in the calculation

$$U = U_{\text{Sk}} + U_{\text{Sym}}. \quad (1)$$

The contributions to the potential energy is given in terms of the density as

$$U_{\text{Sk}} = A \left(\frac{\rho_B}{\rho_0} \right) + B \left(\frac{\rho_B}{\rho_0} \right)^\tau, \quad (2)$$

where ρ_B is the net-baryon density, $\rho_0 = 0.168 \text{ fm}^{-3}$ is the nuclear ground-state density, and A , B , and τ are parameters. Furthermore,

$$U_{\text{Sym}} = \pm 2S_{\text{pot}} \frac{\rho_{I_3}}{\rho_0}, \quad (3)$$

where ρ_{I_3} is the density of the relative isospin projection I_3/I , the sign is positive for positive isospin and negative for negative isospin of the particle of interest.

Since the potentials are not written in a covariant form, they have to be evaluated in the local rest frame for a Lorentz-invariant treatment. In practice, the calculation is performed in an arbitrary calculation frame such as the fixed-target or center-of-mass frame. Therefore, a boost needs to be introduced which results in the following form for the force acting on a particle in the calculation frame:

$$\vec{F} = \frac{\partial U_{\text{Sk}}}{\partial \rho_B} [-(\vec{\nabla} \rho_B + \partial_t \vec{j}_B) + \dot{\vec{x}} \times (\vec{\nabla} \times \vec{j}_B)] + \frac{\partial U_{\text{Sym}}}{\partial \rho_{I_3}} [-(\vec{\nabla} \rho_{I_3} + \partial_t \vec{j}_{I_3}) + \dot{\vec{x}} \times (\vec{\nabla} \times \vec{j}_{I_3})]. \quad (4)$$

\vec{j}_B and \vec{j}_{I_3} are the net-baryon current and the I_3 current, respectively, and $\dot{\vec{x}}$ is the velocity of the particle of interest. Given the force in the calculation frame, the spatial components p_i of the particle momentum are updated at each time step

$$p_i \rightarrow p_i + F_i \Delta t. \quad (5)$$

The calculation therefore relies on small time steps.

Since the potentials and the equations of motion depend on the densities and their spatial derivatives, a high resolution in the density is necessary. In the calculations with potentials within this work, each particle is represented by 20 test particles for a more precise estimate of the densities and their derivatives. The four-current is calculated with the test-particle ansatz

$$j^\mu(r) = \int \frac{p^\mu}{p^0} f(\vec{r}, \vec{p}) d^3 p, \\ f(\vec{r}, \vec{p}) = \sum_{\text{part}} \delta^3(\vec{p} - \vec{p}_{\text{part}}) \delta^3(\vec{r} - \vec{r}_{\text{part}}), \quad (6)$$

where the index part always refers to the test particle under consideration. For numerical calculations, the delta distribution in coordinate space $\delta^3(\vec{r} - \vec{r}_{\text{part}})$ is replaced by a Gaussian smearing Kernel $K(\vec{r} - \vec{r}_{\text{part}})$ in a covariant form as described in Ref. [41] to obtain a smooth density profile

$$K(\vec{r}) = (2\pi\sigma^2)^{-3/2} \gamma \exp\left(-\frac{\vec{r}^2 + (\vec{r} \cdot \vec{u})^2}{2\sigma^2}\right). \quad (7)$$

Here, \vec{u} refers to the spatial part of the four-velocity of the test particle. The application of additional smearing kernels for the test particles is not unique to SMASH but has been applied widely in other Boltzmann-Uehling-Uhlenbeck approaches, as summarized in Table 2 of Ref. [36]. The smearing kernel introduces the smearing width σ as an additional parameter of the model. For all presented calculations the value is set to $\sigma = 1.0 \text{ fm}$ and, in Appendix C, the results are compared with a calculation with a smaller smearing width where a weak

TABLE I. Parameter sets for Skyrme potential with corresponding compressibilities K .

	Soft	Default	Hard
A	-356 MeV	-209.2 MeV	-124 MeV
B	303 MeV	156.4 MeV	71 MeV
τ	1.17	1.35	2.0
K	200 MeV	240 MeV	375 MeV

dependence on σ is observed. For the straight line propagation according to the Hamilton's equation of motion all particles are considered to be pointlike. Due to the smearing of the test particles, our approach constitutes an approximate solution to the Boltzmann equation.

Different sets for the parameters of the Skyrme potential are described in Ref. [42]. They are labeled soft and hard corresponding to their stiffness. In addition, we include the default parameter set in SMASH [36], which lies between the soft and hard one in terms of stiffness. The parameter sets are explicitly given in Table I.

In the future one should aim for a more continuous variation of parameters to find the best values based on experimental data within a Bayesian multiparameter analysis. The momentum dependence will need to be added and the implementation of relativistic mean fields based on density-functional theory is work in progress [37]. In the current work, we do not aim yet at a quantitative extraction of the nuclear equation of state, but would like to provide a baseline for further studies and investigate the influence of light cluster formation.

B. Clustering and light nuclei

At low beam energies, many protons are bound into light nuclei [22]. Therefore, light nuclei formation needs to be taken into account from the theory side to be comparable with experiments. We assume here that deuterons can be produced if two test particles scatter or by coalescence between two test particles. One option to do so is to employ a coalescence model. Here one can calculate the spectrum of nuclei given the proton spectra. A similar approach is to perform clustering on a microscopic basis in each event separately also using the distance in phase space as a criterion for coalescence (see Refs. [29,43]). Finally, one can explicitly form nuclei through production cross sections from hadrons and treat the nuclei dynamically as active degrees of freedom as described in Sec. II C.

In the default SMASH setup, light nuclei are not treated explicitly as degrees of freedom. Instead they are made up of individual nucleons that interact via nuclear potentials. Despite the potentials, nucleons do not form stable bound states in the final state of a heavy-ion collision since the test particles carry only a fraction of the charge of a nucleon and interact through a mean field. We therefore follow the method of identifying light nuclei as described in Refs. [29,43], where the condition for two particles to form a cluster is a small distance in both momentum and coordinate space in the center-of-mass frame of the two particles

at the time where the last interaction occurs in which one of the two particles took part. Compared with the simple clustering algorithm used in Ref. [32], the main difference is the time at which the coordinate space distance of particles is evaluated. The threshold for the momentum and position distances cannot be adopted from Ref. [15], where the same method was used for a similar study, since the particles are not represented by multiple test particles in that work and the average distance in phase space is therefore not comparable. Instead, new thresholds r_0 and p_0 in coordinate and momentum space are found based on the proton rapidity spectrum at 1.23A GeV using Bayesian parameter estimation where the values $r_0 = 0.87^{+0.03}_{-0.03}$ fm and $p_0 = 0.43^{+0.03}_{-0.02}$ GeV are found. We note that the value for r_0 is considerably smaller than the size of a deuteron. Since all cross sections are scaled down by the number of test particles, a smaller clustering radius is reasonable.

C. Deuterons in SMASH

A second option to consider the formation of light nuclei was introduced in Ref. [38] and successfully applied to describe the centrality dependence of deuteron formation at LHC energies [44] as well as the energy dependence [45]. The idea is to explicitly implement cross sections for nuclei production and treat the nuclei as active degrees of freedom as previously done in Refs. [30,46]. The relevant processes for deuteron formation including protons p , neutrons n , pions π , and generic nucleons N are

$$pnN \leftrightarrow dN, \quad (8)$$

$$pn\bar{N} \leftrightarrow d\bar{N}, \quad (9)$$

$$pn\pi \leftrightarrow d\pi, \quad (10)$$

$$NN \leftrightarrow d\pi. \quad (11)$$

The first two are $3 \leftrightarrow 2$ processes that are in practice realized with $2 \leftrightarrow 1$ and $2 \leftrightarrow 2$ processes since multiparticle interactions are not yet present in SMASH. For the intermediate step, a fictional dibaryon resonance $d' \leftrightarrow pn$ is used that can react in $2 \leftrightarrow 2$ processes to a deuteron like $Nd' \leftrightarrow Nd$ or $\pi d' \leftrightarrow \pi d$. Note that the implementation of the backward reactions means that deuterons are continuously formed and destroyed.

To investigate the relevant processes for deuteron formation, Fig. 1 shows the relative number of reaction partners of the d' resonance in percent in gold-gold collisions at $E_{\text{kin}} = 1.23A$ GeV. The numbers do not sum up to 100% because, in many cases, the d' decays without a collision partner. The nucleons clearly dominate the reaction partners, so the $pnN \leftrightarrow dN$ process is, as expected, the most important at this energy [46].

At higher energies, the most important process is the one involving a pion [38]. This difference is caused by the fact that, at higher energies, more pions are produced, while at low energies a dense medium of nuclear matter is produced.

In this work, we compare the simple coalescence approach with the explicit deuteron formation to investigate which description is favored by the experimental data on

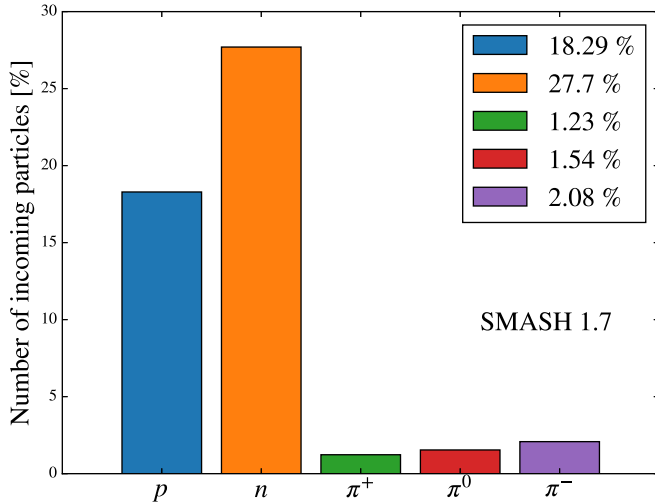


FIG. 1. Relative number of reaction partners of the fictional d' resonance in gold-gold collisions at $E_{\text{kin}} = 1.23A$ GeV. d' often decays into pn without a collision partner, therefore the numbers do not sum to 100%.

flow measurements. The two approaches differ in the sense that the coalescence takes the formation of arbitrary clusters into account while at this point the explicit formation of only deuterons is implemented. It is possible to extend the model also to larger nuclei but the complexity of the problem increases with mass number. Recently, a different way of dynamically forming light nuclei was presented, where a clustering algorithm is applied at each time step of a QMD calculation to identify nuclei instead of producing nuclei in scatterings [31,47]. An advantage of this model is that the formation of larger clusters can be described.

In Fig. 2 a comparison of the two methods in terms of the p_T spectra of nucleons is shown. The curve labeled “no clustering” refers to a calculation without dynamic deuterons and

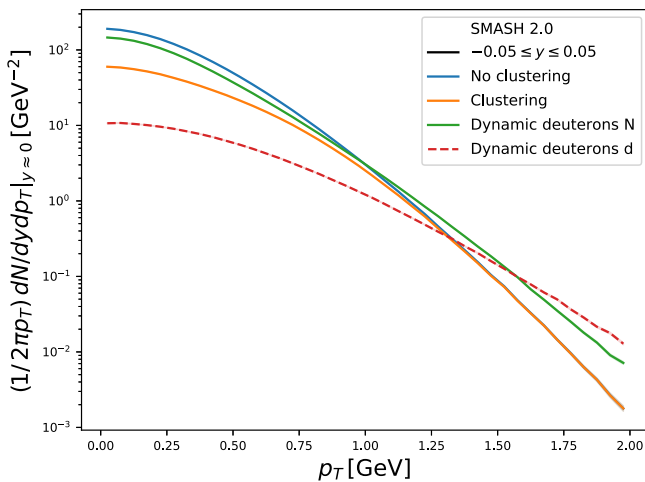


FIG. 2. Transverse momentum spectra of nucleons (full lines) and deuterons (dashed lines) at midrapidity in 20%–30% central gold-gold collisions at $E_{\text{kin}} = 1.23A$ GeV. For all calculations the hard equation of state is used.

without clustering. Naturally, the number of nucleons is the largest in this case. The clustering result has the lowest number of nucleons because the formation of different light nuclei can be taken into account as compared with the dynamic deuteron calculation. The clustering mainly affects the low-momentum part of the spectrum, where the density in phase space is large. Comparing the dynamic treatment of deuterons to the other curves, one can see that the deuteron production influences the dynamics of nucleons significantly as nucleons are shifted to larger p_T . This is related to interactions with deuterons that also have large transverse momentum on average.

D. Flow calculations

In the following we present results for the flow coefficients of protons and deuterons and compare with experimental data [34,35]. To be consistent with the measurement, the flow coefficients are evaluated with respect to the reaction plane, which is fixed to the x - z plane in the calculation setup. Hence, using the angle $\phi = \arctan(p_y/p_x)$, the n th order flow coefficient can be evaluated as an average over particles

$$v_n = \langle \cos(n\phi) \rangle. \quad (12)$$

The centrality of the events is selected by constraining the impact parameter to a specific range. We focus on the 20% to 30% most central gold-gold collisions, which correspond to the impact-parameter range $6.6 \text{ fm} < b < 8.1 \text{ fm}$ [48].

III. DIRECTED FLOW OF PROTONS AND DEUTERONS

We begin with the first-order flow coefficient of protons and deuterons in gold-gold collisions at $E_{\text{kin}} = 1.23A$ GeV. The selection of rapidity and transverse momentum bins is chosen to cover a wide region in phase space. Since flow coefficients in general are sensitive to the strength of the potentials, results from calculations using different equations of state as introduced in Sec. II A are compared. Figure 3 shows the v_1 of nucleons as a function of rapidity for different bins in transverse momentum. The shape reproduces the experimental measurements very well but only the calculation with the hard equation of state gives the correct magnitude. Two calculations consider the formation of light nuclei by clustering in the final state as described in Sec. II B. In addition to the two equations of state, a third calculation is shown, where no clustering is performed but the deuterons are explicitly propagated as degrees of freedom in the calculation as described in Sec. II C. For that calculation, also the hard equation of state is used.

Figure 4 shows the directed flow as a function of transverse momentum for different rapidity bins. Also as a function of p_T , the hard equation of state describes the experimental data best. The difference between the two options to account for nuclei formation is clearly visible at low transverse momentum but vanishes at larger p_T . The importance of clustering in the low-momentum region can be explained by the large phase-space density that makes the formation of nuclei more likely. Compared with the data, clustering gives the best description and produces a small kink in the low- p_T region,

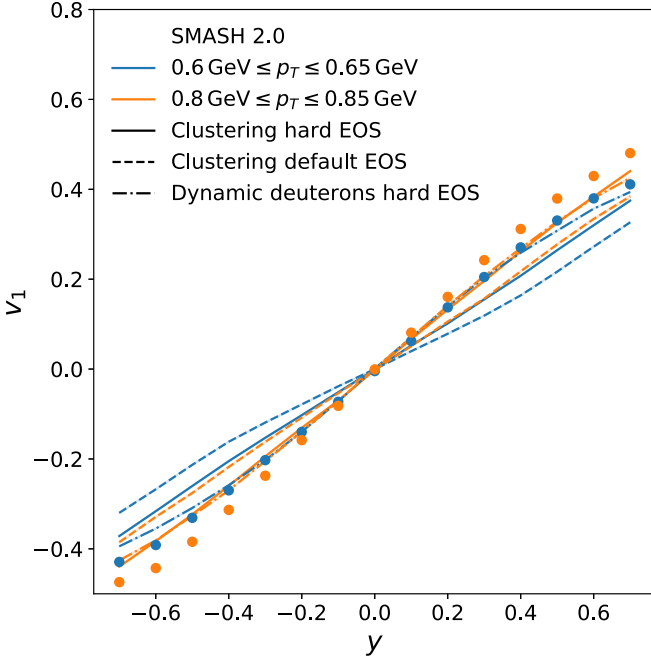


FIG. 3. Directed flow of protons as a function of rapidity in 20%–30% central gold-gold collisions at $E_{\text{kin}} = 1.23A$ GeV for different p_T bins compared with experimental data points [34]. The full lines are obtained with a hard equation of state while, for the dashed lines, the default equation of state is used.

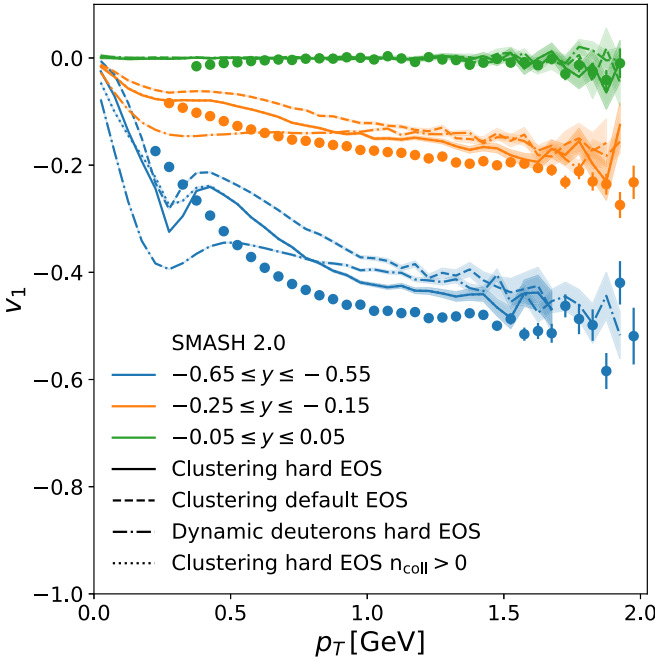


FIG. 4. Directed flow of protons as a function of transverse momentum in 20%–30% central gold-gold collisions at $E_{\text{kin}} = 1.23A$ GeV for different rapidity bins compared with experimental data points [34]. The full lines are obtained with a hard equation of state while, for the dashed lines, the default equation of state is used. The curve labeled “No clustering” takes the formation of light nuclei into account by explicitly producing deuterons during the collision, as described in Sec. II C.

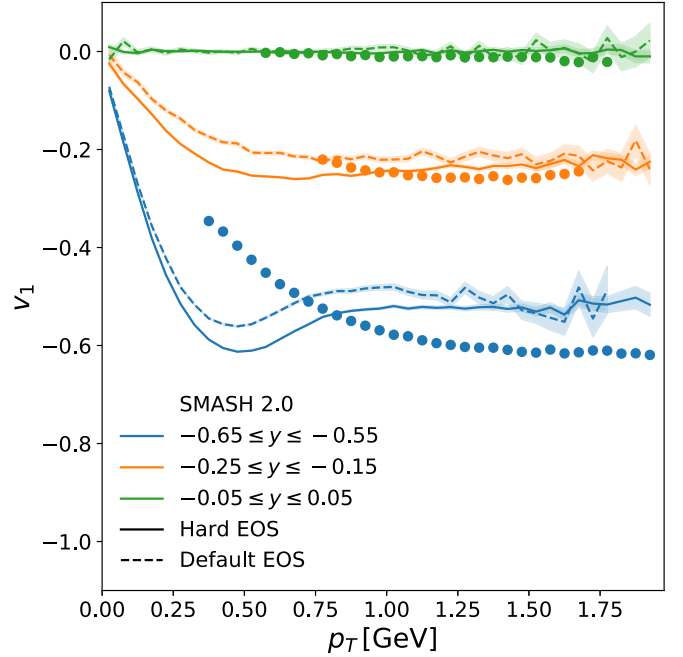


FIG. 5. Directed flow of deuterons as a function of transverse momentum in 20%–30% central gold-gold collisions at $E_{\text{kin}} = 1.23A$ GeV for different rapidity bins compared with experimental data points [34]. A hard equation of state was employed here and deuterons were dynamically treated as particles in this calculation.

while the explicit deuterons give a reasonable description of the data and the curve is more smooth but does not follow the data as closely. The dotted lines are the same as the full lines with the hard equation of state and clustering except all spectators, defined by the criterion that they have not collided, are excluded from the analysis. We observe almost no difference because the spectators are expected to be located more forward in rapidity.

From the calculation where deuterons are explicitly propagated, the directed flow of deuterons themselves is extracted. The results shown in Fig. 5 compare the deuteron flow with the hard and the default equations of state. Considering that the model was originally designed for high-energy collisions where the composition of the system is very different and nuclear potentials are negligible, it is not obvious that the directed flow of deuterons can be described. A reasonable agreement with the experimental data is observed.

To conclude, the findings from the comparison to the measured v_1 , the hard equation of state is clearly favored in this setup. Overall, a good agreement with the data is observed, where the clustering setup follows a bit closer the transverse momentum dependent v_1 of nucleons, and the deuteron flow is matched reasonably well in the calculation with explicit deuteron formation.

IV. ELLIPTIC FLOW OF PROTONS AND DEUTERONS

Continuing with the second-order flow harmonic, Fig. 6 shows the v_2 as a function of rapidity in semicentral gold-gold collisions. Again, two calculations with clustering and differ-

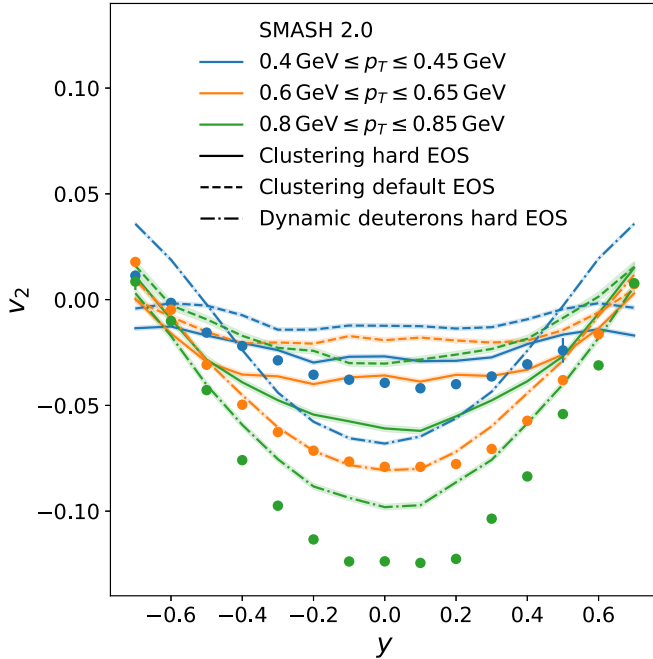


FIG. 6. Elliptic flow of protons as a function of rapidity in 20%–30% central gold-gold collisions at $E_{\text{kin}} = 1.23A$ GeV for different p_T bins compared with experimental data points [34]. The full lines are obtained with a hard equation of state while, for the dashed lines, the default equation of state is used.

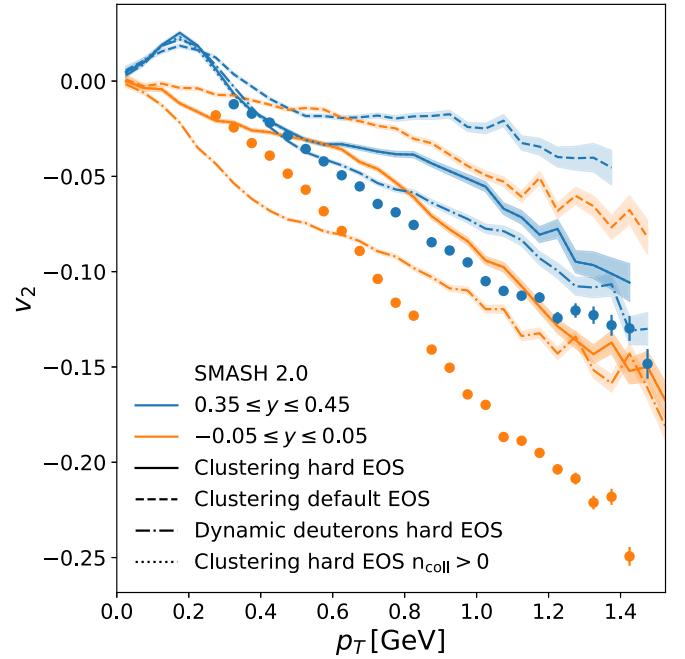


FIG. 7. Elliptic flow of protons as a function of transverse momentum in 20%–30% central gold-gold collisions at $E_{\text{kin}} = 1.23A$ GeV for different rapidity bins compared with experimental data points [34]. The full lines are obtained with a hard equation of state while, for the dashed lines, the default equation of state is used.

ent equations of state and a calculation with explicit deuterons employing a hard equation of state are compared. Naturally, the second-order flow coefficient is more difficult to describe than the first-order one. In general, the magnitude of v_2 is too small at large transverse momenta. However, the flow in the intermediate p_T region, where most nucleons are located, is comparable to the experimental data. Same as for v_1 , the hard equation of state produces a stronger flow signal and is therefore preferred by the data. In addition to that, the magnitude of v_2 is larger when the deuterons are treated explicitly in the calculation. That calculation agrees best with the data. Similar to the observation for v_1 , in the low- p_T region (here the $0.4 \text{ GeV} < p_T < 0.45 \text{ GeV}$ bin) the results are very sensitive to how the formation of light nuclei is taken into account.

The elliptic flow of nucleons as a function of the transverse momentum is shown in Fig. 7. Here it is again rather obvious that the elliptic flow is not well described, especially in the high- p_T region. In the low- p_T region, the clustering performs better, while the calculation with explicit deuteron production works better at intermediate transverse momentum. The difficulties in describing v_2 at high p_T possibly comes from the lack of momentum dependence of the potentials [49].

Figure 8 shows the elliptic flow of deuterons for the calculation, where they are treated as active degrees of freedom. For the hard equation of state, the flow signal is overestimated while the default equation of state is in agreement with the data. Also looking at the p_T differential elliptic flow of deuterons in Fig. 9, the agreement with the data is good only for the default equation of state. Possibly all flow data can be described consistently with more sophisticated potentials.

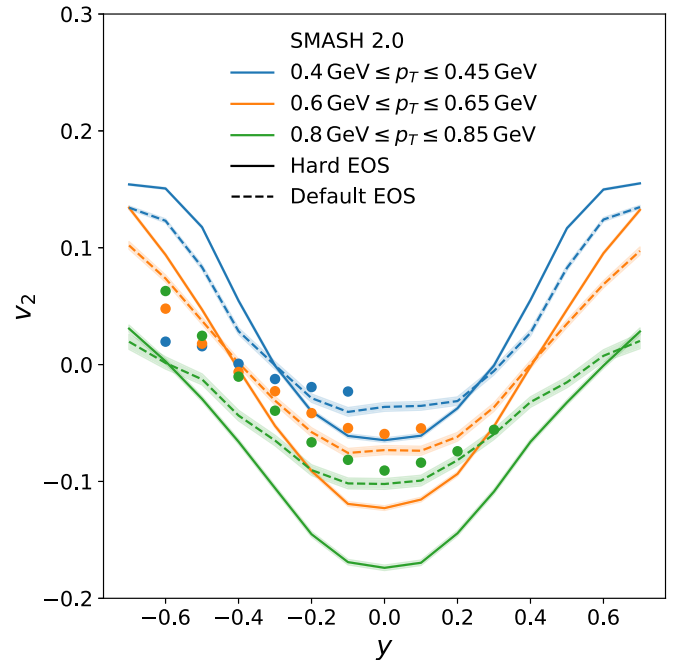


FIG. 8. Elliptic flow of deuterons as a function of rapidity in 20%–30% central gold-gold collisions at $E_{\text{kin}} = 1.23A$ GeV for different transverse momentum bins compared with experimental data points [34]. A hard equation of state was employed here and deuterons were dynamically treated as particles in this calculation.

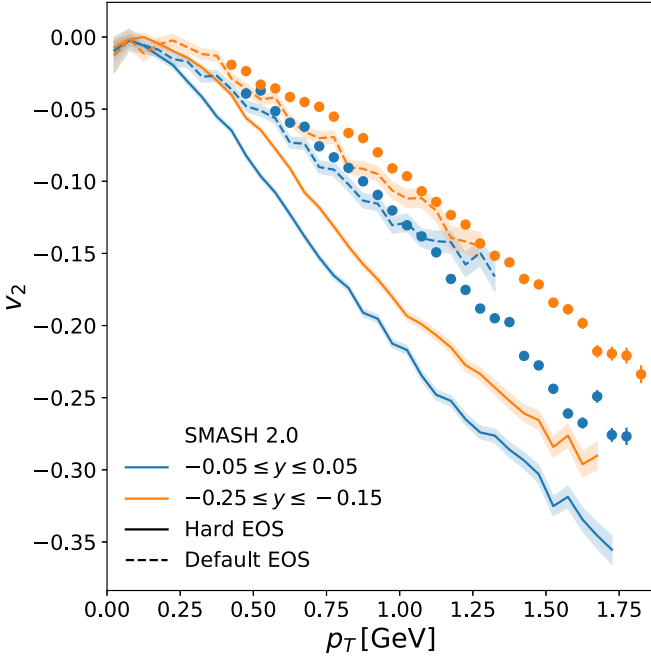


FIG. 9. Elliptic flow of deuterons as a function of transverse momentum in 20%–30% central gold-gold collisions at $E_{\text{kin}} = 1.23A$ GeV for different rapidity bins compared with experimental data points [34]. A hard equation of state was employed here and deuterons were dynamically treated as particles in this calculation.

To conclude this section, the elliptic flow is observed to be very sensitive on how the light nuclei formation is taken into account, which leads to some uncertainty for the extraction of the EoS. The elliptic flow of nucleons at large transverse momenta is underestimated in the SMASH calculations but the best agreement is found with the hard equation of state and treating the deuterons as active degrees of freedom. The fact that the deuteron flow can in this model not be described with the same equation of state hints towards the necessity of improved nuclear potentials.

V. EVOLUTION OF FLOW COEFFICIENTS

In this section we focus on the evolution of flow with time to see when the anisotropy is developed and what the most important stages are. We concentrate on the setting that worked best in comparison to experimental data, namely, the calculation with explicit deuteron formation and a hard equation of state.

The first two panels of Fig. 10 show the multiplicity of nucleons and deuterons respectively as a function of time. The initially present nucleons from the two gold nuclei start interacting, forming resonances and deuterons, so that their number decreases. If no deuterons are present in the calculation, the number of nucleons increases again towards the end of the calculation when all resonances decay. The number of deuterons rises throughout the evolution of the heavy-ion collision. In the third panel one can see the slope of the directed flow at midrapidity as a proxy for the magnitude of v_1 of nucleons and deuterons. To evaluate the slope, at each point

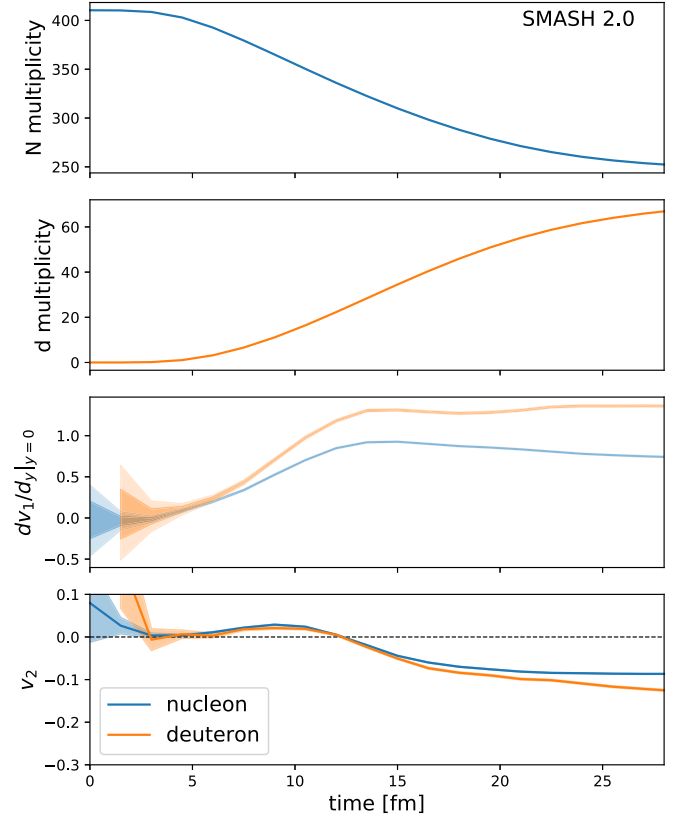


FIG. 10. Nucleon and deuteron multiplicities, slope of the first-order flow coefficient at midrapidity, and v_2 of nucleons and deuterons as a function of time in 20%–30% central gold-gold collisions at $E_{\text{kin}} = 1.23A$ GeV. The flow coefficients are evaluated for particles that satisfy $0.75 \text{ GeV} < p_T < 0.8 \text{ GeV}$ while the number of particles refers to the total multiplicity.

in time the $v_1(y)$ is fit with a function $v_1(y) = ay + by^3$ where the cubic term is added to take the curvature observed in Fig. 3 into account. The fitting is performed by using Bayesian parameter estimation with Markov chain Monte Carlo sampling. The inner band gives a 68% and the outer band a 95% credible interval. At early times the uncertainty is very large since not enough particles have interacted yet and are not located in the relevant phase-space region, and deuterons are not yet produced. Afterward, the flow starts building up from zero to a maximum after ≈ 15 fm. This is the time the nuclei take to pass through each other. Afterward, one observes for both nucleons and deuterons that the flow signal slightly weakens before the deuteron flow increases again and reaches a higher plateau.

The final panel of Fig. 10 compares the elliptic flow at midrapidity between nucleons and deuterons. Once enough particles are produced and located in the investigated kinematic region, the elliptic flows of nucleons and deuterons look almost exactly the same except that the deuteron flow increases further at later times. This is not intuitively clear since no mass number scaling is applied here. Looking at the evolution of v_2 in more detail one can see that, at first, a positive elliptic flow signal starts to build up but soon v_2 drops below zero where it stays until the end of the evolution. Positive elliptic flow is typically associated with pressure gradients

in the initial state. At low collision energies a competing effect is the squeeze out that results in a negative v_2 signal when the slow spectator nuclei are blocking the path and push particles out of the reaction plane [50]. Both effects contribute to the observed elliptic flow.

It is interesting to note that, especially for nucleons, v_2 shows a very different behavior as a function of time than v_1 . The difficulties in describing the elliptic flow and directed flow with the same parameter set might arise from the two being sensitive to different stages of the evolution.

VI. HIGHER FLOW COEFFICIENTS

A. Scalar product v_3

In this section we would like to quantify the triangularity of heavy-ion collisions to extend the excitation function from that of Ref. [51] down to 1.23A GeV. Unlike for the first and second harmonic, the v_3 signal does not simply emerge from the geometry of the colliding nuclei but rather by fluctuations in the overlap region. To really quantify the triangularity of an event it is therefore not sufficient to calculate the flow coefficient with respect to the reaction plane. Hence, for evaluating the triangular flow in this section, the scalar product method [52] is employed because, even though the HADES Collaboration only measures v_3 with respect to the reaction plane, we would like to explore if there is a finite triangular flow in our calculations at low beam energies (see Appendix A for higher-order flow coefficients with respect to the reaction plane).

In the scalar product method the n th flow coefficient is calculated as follows:

$$v_n = \frac{\langle \vec{u} \cdot \frac{\vec{Q}_n}{N} \rangle}{\sqrt{\langle \frac{\vec{Q}_n^A}{N_A} \cdot \frac{\vec{Q}_n^B}{N_B} \rangle_E}}, \quad (13)$$

where \vec{u} is the momentum unit vector of a particle in the transverse plane, $\langle \dots \rangle$ denotes the average over all particles of interest while $\langle \dots \rangle_E$ is an average over events. N is the total number of particles and N_A and N_B are the number of particles in the subevents A and B, respectively. The same labeling applies for the flow vectors \vec{Q}_n^A , \vec{Q}_n^B , and \vec{Q}_n defined as

$$\vec{Q}_n = \left(\sum_i w_i \cos(n\phi_i), \sum_i w_i \sin(n\phi_i) \right), \quad (14)$$

where ϕ_i is the azimuthal angle of particle i , w_i is the weight for the v_3 calculation p_T^3 . The sum runs over the particles in the (sub-)event but, for the scalar product in the numerator of Eq. (13), the particle of interest needs to be excluded from the flow vector calculation to avoid autocorrelations. Each event is divided into subevents according to the pseudorapidity η of the particles. One subevent contains all particles with $\eta > 0.1$ while the other one has particles that satisfy $\eta < -0.1$.

Applying the scalar product method to extract the triangular flow of nucleons one obtains the results shown in Fig. 11. Looking at the scale of the axis the triangular flow signal in collisions at low energies almost vanishes. That agrees with the findings from Ref. [51] where the triangular flow signal vanishes at low collision energies. With

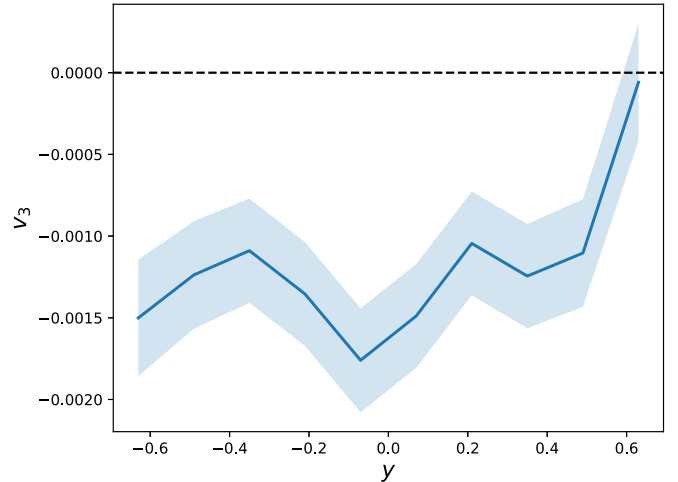


FIG. 11. Triangular flow of nucleons as a function of rapidity in 20%–30% central gold-gold collisions. The flow coefficient is obtained using the scalar product method.

the same cuts ($0.2 \text{ GeV} < p_T < 2.0 \text{ GeV}$ and $|\eta| < 1$) applied as in Ref. [51] we obtain for nucleons and deuterons $v_3 = 0.00081 \pm 0.00006$ and $v_3 = -0.0014 \pm 0.0002$, respectively.

B. Quadrangular flow

In this section we show the fourth-order flow coefficient of nucleons divided by the squared elliptic flow because this quantity is suggested to be a probe of ideal hydrodynamic behavior of the system if $v_4/v_2^2 \approx 0.5$ [53]. v_4/v_2^2 is calculated at midrapidity as a function of p_T and the result is shown in Fig. 12. One can see that v_4/v_2^2 is close to 0.5 in the p_T region above 0.75 GeV. In general, the shape of the curve is similar to the ideal three-dimensional hydro prediction at RHIC energies from Ref. [53] so the pure transport calculation as presented in this work shows in terms of this observable a

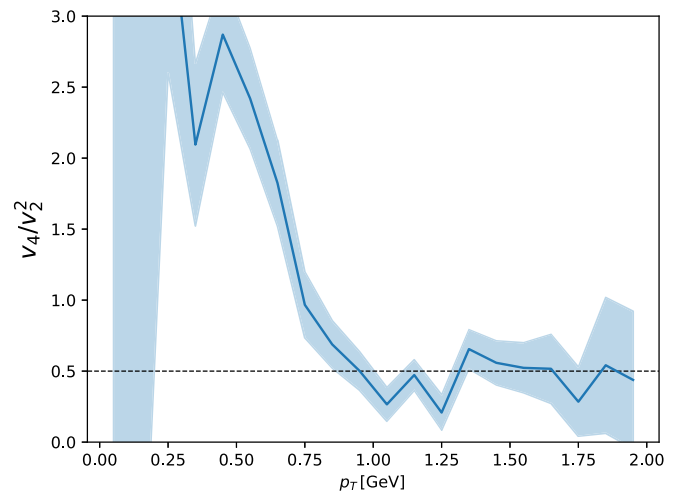


FIG. 12. Quadrangular flow of nucleons divided by the squared elliptic flow at midrapidity as a function of transverse momentum in 20%–30% central gold-gold collisions at $E_{\text{kin}} = 1.23A \text{ GeV}$.

close to hydrodynamic behavior. This is a sign that, in low-energy collisions, the response to the initial geometry within a transport approach is translated as efficiently to final-state observables as expected from a hydrodynamic picture.

VII. CONCLUSIONS AND OUTLOOK

In this paper we compared the double-differential directed and elliptic flow of protons and deuterons to experimental flow measurements in Au + Au collisions at $E_{\text{lab}} = 1.23A$ GeV as provided by the HADES Collaboration. Different parameter sets for the Skyrme potential, which each correspond to a different equation of state, are employed. In our calculation for the flow of both nucleons and deuterons a hard equation of state is preferred by the data. With the currently implemented potentials, the elliptic flow of nucleons and deuterons is not consistently described. Therefore, more sophisticated potentials, including a momentum dependence, will be necessary to extract the equation of state from flow measurements.

The main focus of the current work is the formation of light nuclei in low-energy heavy-ion collisions that cannot be neglected even considering just the flow of nucleons. Two different ways of taking the formation of deuterons into account are implemented. Within this model we observe that dynamically forming deuterons and propagating them as particles throughout the calculation performs better with respect to the HADES data than forming deuterons via coalescence in the final state of a heavy-ion collision. In the setup with the dynamic treatment of deuterons the evolution of the multiplicity and flow of nucleons and deuterons over time is studied. Here one can see that the flow of nucleons and deuterons show a very similar time dependence, while the directed and elliptic flow coefficients are sensitive to different stages in the evolution.

Finally, we show that the scalar product triangular flow of nucleons almost vanishes in collisions at low energy and confirm that $v_4/v_2^2 \approx 0.5$ outside the low- p_T region within the SMASH transport approach.

In the future, a more advanced description of the nuclear potentials [37] will allow for a more detailed comparison to a much broader set of experimental measurements. That comparison can be performed more systematically using Bayesian methods to put reliable constraints on the equation of state.

ACKNOWLEDGMENTS

Discussions and provision of experimental data is acknowledged to Behruz Kardan and Christoph Blume. J.M. acknowledges funding by GSI F&E program and the support by the State of Hesse within the Cluster Project ELEMENTS. Computational resources have been provided by the Center for Scientific Computing (CSC) at the Goethe University and the GSI GreenCube. M.M. acknowledges support by the Deutsche Forschungsgemeinschaft (DFG) through the grant CRC-TR 211 ‘‘Strong-interaction matter under extreme conditions.’’ M.M. would also like to thank Mathilde Ziegler-Himmelreich for fruitful discussions. This article is part of a project that has received funding from the European Union’s

Horizon 2020 research and innovation program under Grant Agreement No. STRONG - 2020 - No 824093.

APPENDIX A: REACTION PLANE v_3 AND v_4

For completeness we provide the triangular and quadrangular flow with respect to the reaction plane in the same p_T bin as shown in Ref. [35]. The hard equation of state is employed for all calculations in this Appendix. Figure 13 shows the first four flow coefficients of nucleons as a function of rapidity. Compared is a calculation with explicit deuteron formation as described in Sec. II C with final-state clustering of nucleons (Sec. II B).

We also provide the four-lowest-order flow coefficients calculation for deuterons in Fig. 14. The deuterons are explicitly produced and propagated throughout the calculation.

APPENDIX B: DEPENDENCE ON TEST PARTICLE NUMBER

This work focuses on the equation of state which is related to the calculation by the nuclear potentials. As mentioned in Sec. II A, the mean fields are expressed in terms of densities and their derivatives and hence rely on the density to be smooth and statistical fluctuations to be under control.

In the following we investigate the dependence on the number of test particles, N_{test} used in the calculation to represent a physical particle by repeating the previous calculations for directed and elliptic flow. The result for the directed and elliptic flow of nucleons in the calculation, where deuterons are explicitly propagated, is shown in Figs. 15 and 16, respectively. The results for one and five test particles are basically identical. However, upon increasing the number of test particles to twenty, a significant difference can be observed for both v_1 and v_2 . Compared with the calculation with twenty test particles, doubling the number of test particles does not lead to a difference in the flow coefficients. For completeness, the

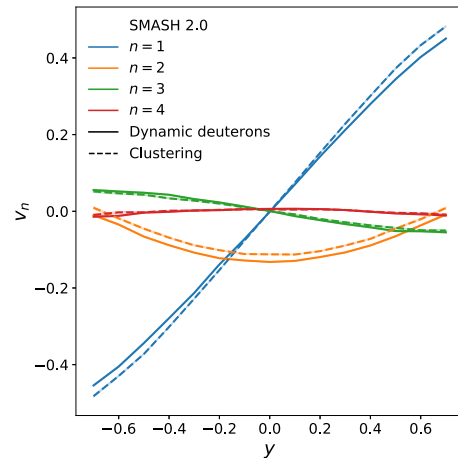


FIG. 13. v_1 to v_4 of nucleons as a function of rapidity in 20%–30% central gold-gold collisions at $E_{\text{kin}} = 1.23A$ GeV for $1.0 \text{ GeV} < p_T < 1.5 \text{ GeV}$. All lines are obtained with a hard equation of state. Compared is a calculation with explicit deuteron formation and clustering.

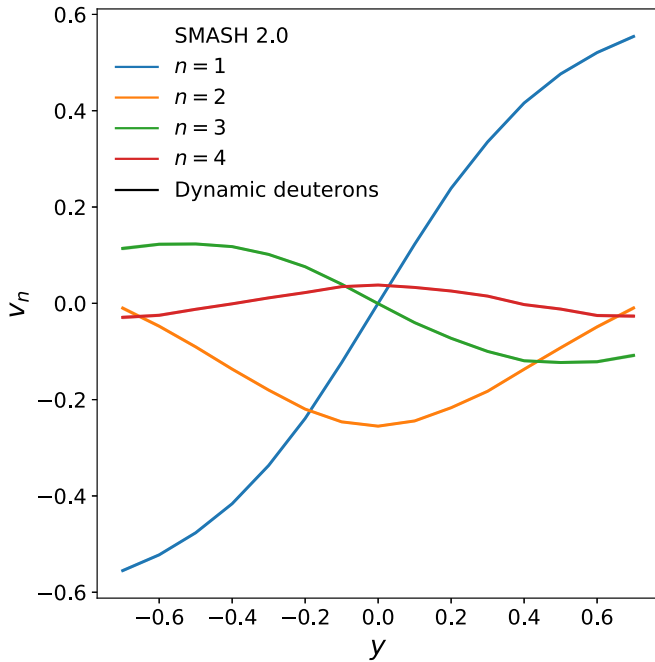


FIG. 14. v_1 to v_4 of deuterons as a function of rapidity in 20%–30% central gold-gold collisions at $E_{\text{kin}} = 1.23A$ GeV for $1.0 \text{ GeV} < p_T < 1.5 \text{ GeV}$. All lines are obtained with a hard equation of state.

same consistency check has been performed for the directed and elliptic flow of deuterons, where the same dependence on the number of test particles was found so the plots are omitted

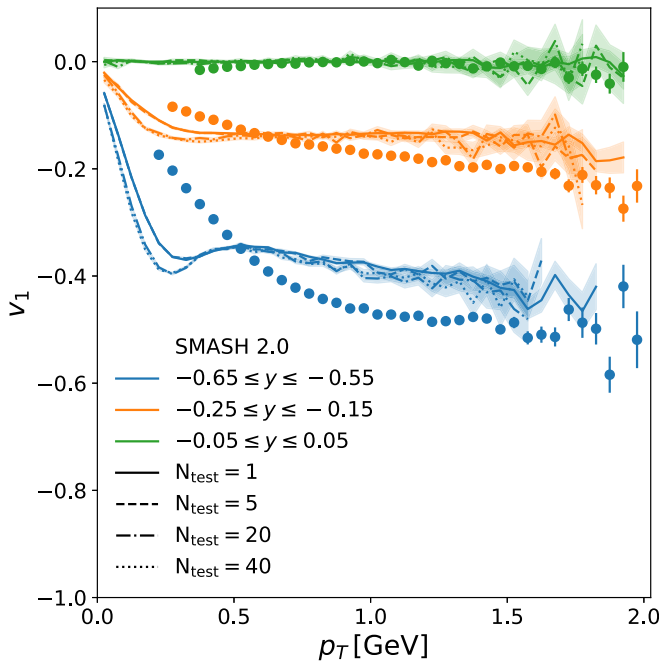


FIG. 15. Directed flow of nucleons as a function of transverse momentum in 20%–30% central gold-gold collisions at $E_{\text{kin}} = 1.23A$ GeV for different rapidity bins compared with experimental data points [34]. Compared are calculations where each particle is represented by a different number of test particles, N_{test} .

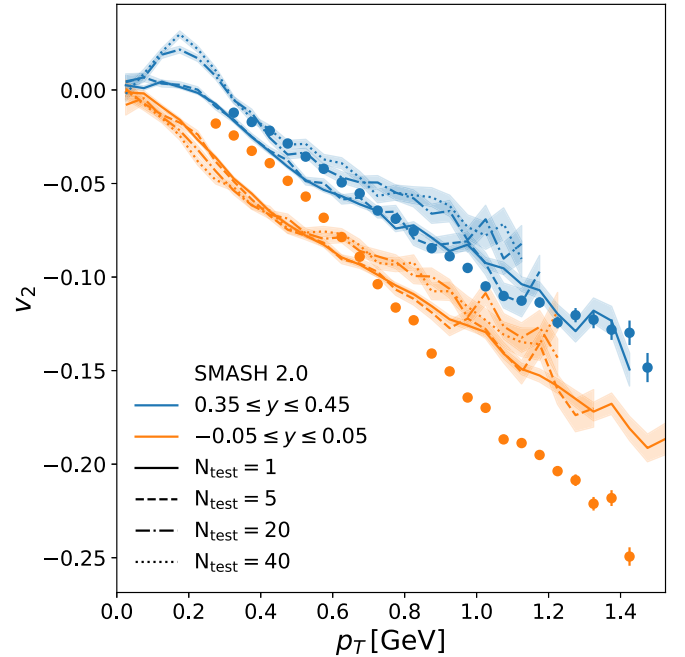


FIG. 16. Elliptic flow of nucleons as a function of transverse momentum in 20%–30% central gold-gold collisions at $E_{\text{kin}} = 1.23A$ GeV for different rapidity bins compared with experimental data points [34]. Compared are calculations where each particle is represented by a different number of test particles, N_{test} .

here. We conclude that representing each particle by twenty test particles is sufficient for a stable calculation of the density and the derivatives of it.

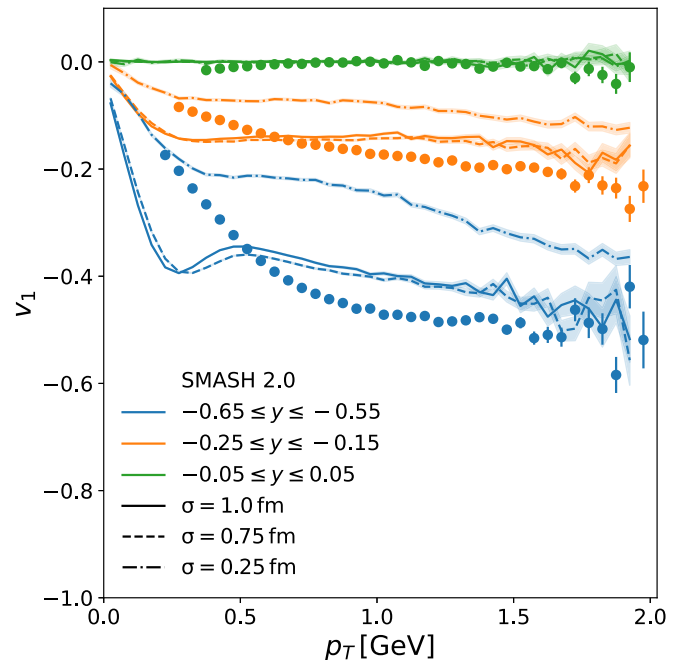


FIG. 17. Directed flow of nucleons as a function of transverse momentum in 20%–30% central gold-gold collisions at $E_{\text{kin}} = 1.23A$ GeV for different rapidity bins. Three calculations with different smearing widths are compared.

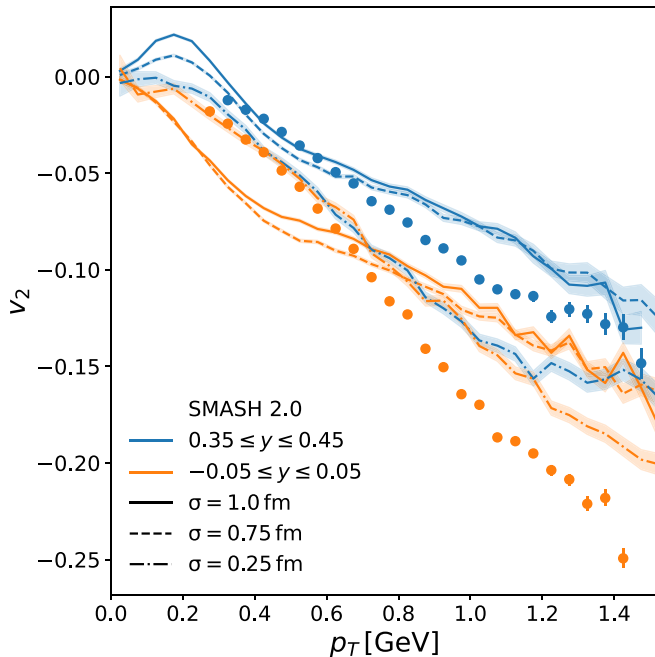


FIG. 18. Elliptic flow of nucleons as a function of transverse momentum in 20%–30% central gold-gold collisions at $E_{\text{kin}} = 1.23A$ GeV for different rapidity bins. Three calculations with different smearing widths are compared.

The reason for the relatively low number of required test particles to obtain a reliable mean-field calculation is that

each particle is smeared in coordinate space as described in Ref. [41].

APPENDIX C: DEPENDENCE ON SMEARING WIDTH

For the results presented in this work, a smearing kernel is applied to each test particle for calculating the densities required for the evaluation of the potentials. The specific form of the covariant Gaussian smearing that was used is introduced in Ref. [41]. By applying the Gaussian smearing one can efficiently calculate the density with a moderate number of test particles, as described in the previous section. However, the smearing introduces a free parameter to the model that is the smearing width σ of the Gaussian. The smearing parameter is set to $\sigma = 1.0$ fm for all results presented in this and all previous papers involving SMASH calculations. This number is chosen to be similar to the size of a proton which is the main contribution to the baryon density. In Figs. 17 and 18 the results for v_1 and v_2 for nucleons obtained with $\sigma = 1.0$ fm are compared with $\sigma = 0.75$ fm and $\sigma = 0.25$ fm. One can see a significant dependence on the smearing width. However, the difference between $\sigma = 1.0$ fm and $\sigma = 0.75$ fm is small enough so that the conclusions from this work would still hold for $\sigma = 0.75$ fm. For $\sigma = 0.25$ fm the difference is large. The reason for this difference is that the width is in this case too small and no smooth density profile can be obtained with only 20 test particles. For a more clear comparison the number of test particles is kept equal throughout this plot but a better agreement between the calculations is expected with a larger number of test particles.

- [1] W. Scheid, H. Muller, and W. Greiner, *Phys. Rev. Lett.* **32**, 741 (1974).
- [2] P. Danielewicz, R. Lacey, and W. G. Lynch, *Science* **298**, 1592 (2002).
- [3] J. Aichelin, A. Rosenhauer, G. Peilert, H. Stoecker, and W. Greiner, *Phys. Rev. Lett.* **58**, 1926 (1987).
- [4] C. Gale, G. Bertsch, and S. Das Gupta, *Phys. Rev. C* **35**, 1666 (1987).
- [5] W. Reisdorf *et al.* (FOPI Collaboration), *Nucl. Phys. A* **876**, 1 (2012).
- [6] M. Isse, A. Ohnishi, N. Otuka, P. K. Sahu, and Y. Nara, *Phys. Rev. C* **72**, 064908 (2005).
- [7] A. Le Fèvre, Y. Leifels, W. Reisdorf, J. Aichelin, and C. Hartnack, *Nucl. Phys. A* **945**, 112 (2016).
- [8] A. Le Fèvre, Y. Leifels, C. Hartnack, and J. Aichelin, *Phys. Rev. C* **98**, 034901 (2018).
- [9] C. Hartnack, H. Oeschler, and J. Aichelin, *Phys. Rev. Lett.* **96**, 012302 (2006).
- [10] J. J. Molitoris, D. Hahn, and H. Stoecker, *Nucl. Phys. A* **447**, 13 (1986).
- [11] J. J. Molitoris and H. Stoecker, *Phys. Rev. C* **32**, 346 (1985).
- [12] G. F. Bertsch and S. Das Gupta, *Phys. Rep.* **160**, 189 (1988).
- [13] H. Petersen, Q. Li, X. Zhu, and M. Bleicher, *Phys. Rev. C* **74**, 064908 (2006).
- [14] P. Hillmann, J. Steinheimer, and M. Bleicher, *J. Phys. G* **45**, 085101 (2018).
- [15] P. Hillmann, J. Steinheimer, T. Reichert, V. Gaebel, M. Bleicher, S. Sombun, C. Herold, and A. Limphirat, *J. Phys. G* **47**, 055101 (2020).
- [16] Y. Nara, H. Niemi, J. Steinheimer, and H. Stöcker, *Phys. Lett. B* **769**, 543 (2017).
- [17] B. Abbott *et al.* (LIGO Scientific Collaboration, Virgo Collaboration), *Phys. Rev. Lett.* **116**, 061102 (2016).
- [18] A. Bauswein, Niels-Uwe F. Bastian, D. B. Blaschke, K. Chatziioannou, J. A. Clark, T. Fischer, and M. Oertel, *Phys. Rev. Lett.* **122**, 061102 (2019).
- [19] E. R. Most, L. R. Weih, L. Rezzolla, and J. Schaffner-Bielich, *Phys. Rev. Lett.* **120**, 261103 (2018).
- [20] Y. Wang, Q. Li, Y. Leifels, and A. Le Fèvre, *Phys. Lett. B* **802**, 135249 (2020).
- [21] M. B. Tsang, J. R. Stone, F. Camera, P. Danielewicz, S. Gandolfi, K. Hebeler, C. J. Horowitz, J. Lee, W. G. Lynch, Z. Kohley, R. Lemmon, P. Moller, T. Murakami, S. Riordan, X. Roca-Maza, F. Sammarruca, A. W. Steiner, I. Vidana, and S. J. Yennello, *Phys. Rev. C* **86**, 015803 (2012).
- [22] W. Reisdorf *et al.* (FOPI Collaboration), *Nucl. Phys. A* **848**, 366 (2010).
- [23] S. Butler and C. Pearson, *Phys. Rev. Lett.* **7**, 69 (1961).
- [24] A. Schwarzschild and C. Zupancic, *Phys. Rev.* **129**, 854 (1963).
- [25] H. Gutbrod, A. Sandoval, P. Johansen, A. M. Poskanzer, J. Gosset, W. Meyer, G. Westfall, and R. Stock, *Phys. Rev. Lett.* **37**, 667 (1976).
- [26] J. I. Kapusta, *Phys. Rev. C* **16**, 1493 (1977).

- [27] R. Bond, P. J. Johansen, S. E. Koonin, and S. Garpman, *Phys. Lett. B* **71**, 43 (1977).
- [28] R. Scheibl and U. W. Heinz, *Phys. Rev. C* **59**, 1585 (1999).
- [29] L. Zhu, C. M. Ko, and X. Yin, *Phys. Rev. C* **92**, 064911 (2015).
- [30] Y. Oh, Z.-W. Lin, and C. M. Ko, *Phys. Rev. C* **80**, 064902 (2009).
- [31] J. Aichelin, E. Bratkovskaya, A. Le Fèvre, V. Kireyeu, V. Kolesnikov, Y. Leifels, V. Voronyuk, and G. Coci, *Phys. Rev. C* **101**, 044905 (2020).
- [32] J. Weil, V. Steinberg, J. Staudenmaier, L. G. Pang, D. Oliinychenko, J. Mohs, M. Kretz, T. Kehrenberg, A. Goldschmidt, B. Bauchle, J. Auvinen, M. Attems, and H. Petersen, *Phys. Rev. C* **94**, 054905 (2016).
- [33] D. Oliinychenko, V. Steinberg, J. Weil, M. Kretz, J. Staudenmaier, S. Ryu, A. Schäfer, J. Rothermel, J. Mohs, F. Li, H. E. (Petersen), L. Pang, D. Mitrovic, A. Goldschmidt, L. Geiger, J.-B. Rose, J. Hammelmann, and L. Prinz, *Smash-Transport/Smash: Smash-1.8* (2020), doi: 10.5281/zenodo.4336358.
- [34] B. Kardan (HADES Collaboration), *Nucl. Phys. A* **982**, 431 (2019).
- [35] J. Adamczewski-Musch *et al.* (HADES Collaboration) *Phys. Rev. Lett.* **125**, 262301 (2020).
- [36] J. Xu, L. W. Chen, ManYeeBetty Tsang, H. Wolter, Y. X. Zhang, J. Aichelin, M. Colonna, D. Cozma, P. Danielewicz, Z. Q. Feng, A. LeFevre, T. Gaitanos, C. Hartnack, K. Kim, Y. Kim, C. M. Ko, B. A. Li, Q. F. Li, Z. X. Li, P. Napolitani, A. Ono, M. Papa, T. Song, J. Su, J. L. Tian, N. Wang, Y. J. Wang, J. Weil, W. J. Xie, F. S. Zhang, and G. Q. Zhang, *Phys. Rev. C* **93**, 044609 (2016).
- [37] A. Sorensen and V. Koch, *Phys. Rev. C* **104**, 034904 (2021).
- [38] D. Oliinychenko, L.-G. Pang, H. Elfner, and V. Koch, *Phys. Rev. C* **99**, 044907 (2019).
- [39] M. Tanabashi *et al.* (Particle Data Group), *Phys. Rev. D* **98**, 030001 (2018).
- [40] D. M. Manley and E. M. Saleski, *Phys. Rev. D* **45**, 4002 (1992).
- [41] D. Oliinychenko and H. Petersen, *Phys. Rev. C* **93**, 034905 (2016).
- [42] H. Kruse, B. V. Jacak, and H. Stöcker, *Phys. Rev. Lett.* **54**, 289 (1985).
- [43] S. Sombun, K. Tomuang, A. Limphirat, P. Hillmann, C. Herold, J. Steinheimer, Y. Yan, and M. Bleicher, *Phys. Rev. C* **99**, 014901 (2019).
- [44] D. Oliinychenko, *Nucl. Phys. A* **1005**, 121754 (2021).
- [45] D. Oliinychenko, C. Shen, and V. Koch, *Phys. Rev. C* **103**, 034913 (2021).
- [46] P. Danielewicz and G. Bertsch, *Nucl. Phys. A* **533**, 712 (1991).
- [47] S. Gläsel, V. Kireyeu, V. Voronyuk, J. Aichelin, C. Blume, E. Bratkovskaya, G. Coci, V. Kolesnikov, and M. Winn, *Phys. Rev. C* **105**, 014908 (2022).
- [48] J. Adamczewski-Musch *et al.* (HADES Collaboration), *Eur. Phys. J. A* **54**, 85 (2018).
- [49] G. M. Welke, M. Prakash, T. T. S. Kuo, S. Das Gupta, and C. Gale, *Phys. Rev. C* **38**, 2101 (1988).
- [50] H. Gutbrod, B. Kolb, H. Schmidt, A. M. Poskanzer, H. Ritter, and K. Kampert, *Phys. Lett. B* **216**, 267 (1989).
- [51] I. A. Karpenko, P. Huovinen, H. Petersen, and M. Bleicher, *Phys. Rev. C* **91**, 064901 (2015).
- [52] C. Adler *et al.* (STAR Collaboration), *Phys. Rev. C* **66**, 034904 (2002).
- [53] N. Borghini and J.-Y. Ollitrault, *Phys. Lett. B* **642**, 227 (2006).